J. Plasma Phys. (2026), *vol*. 92, E81 © The Author(s), 2026. Published by Cambridge University Press.
This is an Open Access article, distributed under the terms of the Creative Commons Attribution licence (https://creativecommons.org/licenses/by/4.0/), which permits unrestricted re-use, distribution and reproduction, provided the original article is properly cited. doi:10.1017/S0022377826101846

Solar wind effects on nonlinear electrostatic structures at the Venusian mantle

Ahmed Gamal[1], Waleed M. Moslem[2,3], M. Saleh Yousef[1], A.Y. Ellithi[1] and Shaaban M. Shaaban[4]

[1]Department of Physics, Faculty of Science, Cairo University, Giza 12613, Egypt
[2]Department of Physics, Faculty of Science, Port Said University, Port Said 42521, Egypt
[3]Centre for Theoretical Physics, The British University in Egypt, El-Shorouk City, Cairo 11837, Egypt
[4]Department of Physics and Materials Sciences, College of Arts and Sciences, Qatar University, Doha 2713, Qatar

Corresponding author: Shaaban M. Shaaban, shamd@qu.edu.qa

(Received 11 March 2026 UTC; revision received 10 May 2026 UTC; accepted 14 May 2026 UTC)

Phase-space electron holes, recognised as fundamental nonlinear electrostatic structures in space plasmas, have recently been detected near the mantle boundary of the Venusian magnetosheath by both the Parker Solar Probe (PSP) and the Pioneer Venus Orbiter (PVO). To understand their origin and characteristics, we develop a hydrodynamic model coupled with reductive perturbation theory that incorporates a small population of non-isothermal trapped electrons together with the dynamical effects of solar-wind ions and electrons. This formulation yields a generalised Schamel–Korteweg de Vries equation supporting two distinct classes of nonlinear electrostatic modes: solitary waves and double layers. Using parameter ranges constrained by *in situ* measurements – including relative densities, drift velocities and temperature ratios – we conduct a detailed parametric investigation of both structures. For the solitary-wave solutions, the model predicts electric field amplitudes of $\sim$20 mV m^{-1}, temporal scales of $\sim$(2.5−4.5) ms and characteristic frequencies of $\sim$(0.31−5.6) kHz. The double-layer solutions exhibit fields of $\sim$18 mV m^{-1}, durations of $\sim$4.5 ms and frequencies of $\sim$(0.63−1.6) kHz. These results are in strong agreement with PSP and PVO observations, which report electrostatic fluctuations near 5.4 kHz with amplitudes of $\sim$20 mV m^{-1}. The present analysis therefore provides a consistent physical interpretation of electron-hole structures in the Venusian magnetosheath and highlights their role in mediating kinetic processes at unmagnetised planetary boundaries.

Key words: space plasma physics, plasma waves, plasma nonlinear phenomena

1. Introduction

Venus is comparable to Earth in terms of size, mass and internal composition. However, unlike Earth, Venus lacks an intrinsic global magnetic field, leaving its atmosphere unprotected from the solar wind, which is a continuous stream of charged particles emitted by the Sun. As a result, the upper layers of the Venus

atmosphere, particularly the ionosphere, experience significant atmospheric loss because of direct exposure to this solar wind. The plasma environment of Venus is thus regulated by the joint influence of solar wind and solar radiation, leading to extensive ionisation, plasma instabilities and increased atmospheric loss, e.g. acceleration of ionospheric plasma into space like hydrogen and oxygen, because they are light ions. In the absence of an internal magnetic shield, Venus develops a weak induced magnetosphere. This external magnetic shielding arises from the interaction between the solar wind and the dense ionosphere of the planet. Specifically, the interplanetary magnetic field is draped around Venus by the solar-wind flow, and induced electric currents at the ionospheric boundary give rise to localised magnetic fields that partially mediate the solar-wind interaction (Spenner *et al*. 1980; Futaana *et al*. 2017).

The exploration and investigation of Venus are of profound relevance to our knowledge of planetary formation, climate and atmospheric processes, and are therefore an excellent research target for astronomers and planetary scientists alike (Taylor Jr *et al.* 1980; Luhmann 1986; Bougher, Hunten & Phillips 2022). Several spacecraft missions, such as Venus Express (VEX) and Pioneer Venus Orbiter (PVO), have investigated the effect of the solar wind on the Venus atmosphere in depth (Luhmann *et al*. 1991; Mahajan & Dwivedi 2004; Barabash *et al*. 2007; Futaana *et al*. 2017). Examples of space plasmas that often form collisionless media include ionospheres and magnetospheres. Consequently, other plasma regions gain energy and momentum through plasma waves. They are thus thought to be a crucial aspect of space plasmas. Because space plasma is often in non-thermal equilibrium or contains a significant quantity of free energy, waves have been shown to be widely used everywhere. One of several places in the planet's environment where electrostatic solitary waves are seen is the magnetosheath (Strangeway 1991; Pickett *et al*. 2003). Plasma waves in the Venus mantle (between the magnetosheath and the lobe region) were detected by the Orbiter Electric Field Detector (OEFD) during the PVO mission. During the PVO flyby, several waves were seen, and it was found that the wave observations were in the 100 Hz channel and the Doppler-shifted ion-acoustic waves in the 730 Hz and 5.4 kHz channels. Current research increases the breadth and reliability of studies on wave phenomena in the Venus environment (Scarf *et al.* 1980*b*; Strangeway 1991; Futaana *et al*. 2017; Yadav 2022; Kamalam *et al*. 2023; Rubia *et al*. 2023).

In space plasma, holes are regions where there is a depletion in a specific physical quantity relative to the surrounding areas, such as a density hole, where the number of charged particles is significantly lower than in the surrounding plasma, and a magnetic hole, where the magnetic field is significantly lower than in the surrounding plasma. The electron hole in the phase space is a localised area of positive potential with an electron density lower than that of the surrounding plasma. This occurs as a result of the phase-space density being decreased by constrained electron orbits. A local maximum charge density is caused by a decrease in electron density, which increases the electric potential. This increased potential, in turn, enhances the trapping of electrons in a self-consistent manner, and this leads to the formation of solitary electrostatic waves in a bipolar parallel electric field (Schamel 1986; Franz *et al*. 2005; Hutchinson 2017; Kuzichev *et al*. 2017; Holmes *et al*. 2018; Hadid *et al*. 2021).

Ion-acoustic waves (IAWs) are important in the study of nonlinear phenomena such as turbulence and solitons when modelling complex plasma systems. These waves are low-frequency (relative to electrons) collective excitations that travel in the

https://doi.org/10.1017/S0022377826101846 Published online by Cambridge University Press

plasma medium because of the coupling between electron pressure and ionic inertia. The IAW mechanism is related to the restoring of charge neutrality in the plasma. When a small disturbance compresses the ions in a region, the electrons, since they are much more mobile, redistribute themselves instantaneously to shield the excess positive charge. Their thermal pressure, however, does not allow the shielding to be complete and generates an electrostatic field that pushes the heavier ions back towards equilibrium. This ion movement generates a propagating wave. The IAWs play a key role in numerous plasma processes, such as energy transfer, wave–particle interactions and both space and laboratory plasma dynamics. Electrostatic waves *in situ* detected by the Parker Solar Probe (PSP) in the mantle region of the Venus atmosphere propagate parallel to the magnetic field (with an average magnitude of $B \sim 100$ nT) or, in its absence, along the local plasma direction (Lundin *et al*. 2011; Knudsen *et al*. 2016; Morsi *et al*. 2024). Parallel propagation with respect to the magnetic field implies that the field does not affect the longitudinal electrostatic structure of the waves, but influences only their transverse dynamics. Accordingly, we adopt a one-dimensional model in which the electrostatic wave propagates strictly parallel to the ambient magnetic field. This configuration has been reported in recent observational and theoretical studies (Hadid *et al*. 2021; Rubia *et al*. 2023), providing further support for the validity of this assumption. In the parallel case, the magnetic field does not modify the longitudinal electrostatic dynamics, allowing us to neglect magnetic terms and focus on the fundamental wave behaviour. This simplification is appropriate for the cases analysed here, while the characteristics of magnetised or oblique propagation could be explored in future studies. Various wave phenomena, including 100 Hz electromagnetic whistler waves, 5.4 kHz Doppler-shifted electrostatic IAWs and 30 kHz Langmuir oscillations, have been observed in the Venus generated magnetosphere (Scarf, Taylor & Green 1979, 1980*b*; Strangeway 1991). A phase-space electron hole travelling parallel to the magnetic field is among them; it has a Doppler-shifted frequency of around 5.4 kHz and an electric field of about 15 mV m^{-1}. These results demonstrate how intricate and unpredictable plasma interactions are in the Venus ionosphere (Malaspina *et al*. 2014; Hadid *et al*. 2021; Rubia *et al*. 2023).

A double-layer (DL) or shock-like structure in a plasma is the spontaneous formation of two parallel layers of opposite electrical charges, creating a localised electric field that has the capability to accelerate particles. They are spontaneously formed in a plasma under certain conditions and are responsible for the particle dynamics and energy transfer. Such DLs are usually considered as nonlinear phenomena and can serve as sources of strong electric fields controlling the motion of neighbouring plasma. Using the PSP, electrostatic ion-acoustic DLs were detected in the Venusian magnetosheath (Block 1978; Gołkowski *et al.* 2019; Malaspina *et al*. 2020).

When hot and cold electron populations interact, fascinating plasma structures known as DLs are created. It has been suggested that the mixing of planetary cold electrons with electrons from the solar wind may activate these formations. Because it has the potential to accelerate or heat planetary cold electrons, this excitation process is important because it can affect the dynamics of the surrounding plasma. The contact between hot and cold plasma populations, which fosters the production of DLs, is one of the basic processes causing this excitation. For Venus in particular, these formations are thought to form in the transition zone where the colder planetary plasma interacts with the solar wind. Due to this special configuration, the two plasma populations could interact more easily, which activates DLs and may

https://doi.org/10.1017/S0022377826101846 Published online by Cambridge University Press

be important in determining how the plasma behaves close to the planet (Hultqvist 1971; Knorr & Goertz 1974).

A solitary wave (SW) is a localised disturbance that arises from a delicate balance between nonlinear and dispersive effects, maintaining its shape while propagating at a constant speed. Such waves are generally encountered in plasmas and fluids, where nonlinearity tends to steepen the wave front and dispersion counteracts this tendency by spreading the wave energy. In planetary ionospheres, such as that of Venus, single waves have been suggested as key contributors to plasma dynamics. The ionosphere of Venus is significant in that it can provide some insights into ion outflow and drivers of atmospheric loss. The creation of solitary structures could be the cause of ion acceleration and transport outside the planet-created magnetosphere and could have a role in long-term atmospheric development on Venus (Rosenau 1997; Akbari *et al*. 2022).

In this study, we advance the theoretical description of phase-space electron holes identified in the Venusian mantle, where electrons are confined within localised electrostatic structures, by incorporating the dynamics of trapped ionospheric electrons. To capture the departure of the electron population from a Boltzmann distribution, we adopt a Schamel-type trapping-compatible closure, which introduces modified nonlinear characteristics and supports the existence of both SW and DL solutions. The formulation accounts for the finite nonlinear contribution arising from weak trapping, thereby validating the application of the reductive perturbation method (Scarf *et al*. 1979; Malaspina *et al*. 2020; Hadid *et al*. 2021). The purpose of this work is to investigate the influence of the solar wind on phase-space electron holes that govern the nonlinear evolution of IAWs at the upper mantle barrier, based on temperature, density and velocity measurements obtained by the VEX mission (Lundin *et al*. 2011; Knudsen *et al*. 2016). This treatment complements and extends the approach of Morsi *et al*. (2024), in which they considered Maxwellian fluid electrons and therefore did not include electron-hole effects. Furthermore, the present normalisation, based on oxygen ion species and Venusian mantle temperatures, provides a physically consistent framework that differs from the hydrogen-based, isothermal model employed by Morsi *et al*. (2024), which can be regarded as a limiting case of the more general approach developed here. While both studies employ a Zakharov–Kuznetsov-type formulation, the present model establishes a comprehensive and physically consistent framework for describing nonlinear plasma dynamics in the Venusian environment. The novelty of this work lies in its integration of solar-wind effects with Schamel-type electron trapping in a Venusian plasma context, offering new insights into the formation and evolution of electrostatic structures under realistic planetary conditions.

The structure of the work is arranged as follows. In § 2, we investigate the physical representation of our observations and the hydrodynamic model. In § 3, we evaluate our model using the perturbation method and a small percentage of non-isothermal electron distributions (Schamel distribution). While in § 4, our theoretical study's numerical results are explained. Finally, § 5 presents a summary and conclusion.

2. Formulation of the problem

2.1. *Physical representation and observations*

Physical morphology and observational data of the mantle region of the Venus ionosphere are important in the mediation of solar wind and planetary plasma interaction. The mantle has been described as an intermediate region between the

https://doi.org/10.1017/S0022377826101846 Published online by Cambridge University Press

magnetosheath and the ionosphere with a varying electron energy distribution from planetary to solar wind (Futaana *et al*. 2017).

Despite the importance of this planet, few space missions, such as PVO (Colin 1980) and VEX (Titov *et al.* 2006), were equipped with plasma wave detectors. The OEFD on PVO has poor frequency resolution, and wave modes are not easily detectable (Scarf *et al.* 1980*b*). Despite the other explanations offered (e.g. whistler waves, lower hybrid waves or IAWs), more recent theory and observations identify IAWs as the leading candidate for wave activity observations (Scarf *et al.* 1980*b*; Huba 1993; Strangeway & Crawford 1993). Although Venusian IAW observations are important, we need more high-resolution missions to keep monitoring these waves and the role they play in solar wind–Venusian ionosphere energy and momentum transfer. So we study IAWs (SWs and DLs) to know how the solar wind affects the environmental plasma.

2.2. *Theoretical model*

This paper examines the propagation of electrostatic ion-acoustic excitations through the Venusian mantle. To do so, we use a hydrodynamic model of a one-dimensional, collisionless plasma that includes two adiabatic, positively charged planetary ions, namely hydrogen (subscript H^+) and oxygen (subscript O^+), as well as streaming solar-wind protons (subscript sp). Our model also incorporates inertialess solar-wind thermal and superthermal (Kappa-distributed) electrons (subscripts se and ke, respectively), as well as inertialess, free and trapped planetary electrons (subscripts fe and te).

The continuity and the momentum equations of the ionic species ($j = O^+, H^+, sp$) are given by

$$\frac{\partial n_j}{\partial t} + \frac{\partial (n_j u_j)}{\partial x} = 0,$$
$$\frac{\partial u_j}{\partial t} + u_j \frac{\partial u_j}{\partial x} + \rho_j \frac{\partial \phi}{\partial x} + 3\sigma_j \rho_j n_j \frac{\partial n_j}{\partial x} = 0, \tag{2.1}$$

where $\sigma_j = T_j / T_{eff}$ is the ratio between the j species temperature T_j and the effective electron temperature T_{eff}, and $\rho_j = m_{O^+}/m_j$ is the mass ratio between the O^+ and the j species.

The ionospheric electrons are assumed to be inertialess and consist of a small percentage of non-isothermal trapped electrons (subscript 'te') and isothermal electrons (subscript 'fe') (Schamel 1973; Das, Paul & Karmakar 1986):

$$n_e = \exp(\phi/\sigma_{fe}) - \frac{4}{3} b\, (\phi/\sigma_{te})^{3/2}, \tag{2.2}$$

with

$$b = \frac{1}{\sqrt{\pi}}(1-\beta), \quad \beta = \frac{T_{fe}}{T_{te}}, \quad \sigma_{fe} = \frac{T_{fe}}{T_{eff}}, \quad \sigma_{te} = \frac{T_{te}}{T_{eff}}, \tag{2.3a}$$

$$T_{eff} = \frac{T_{fe} T_{ke} T_{se}\, (\kappa - 3/2)}{\mu\, (\kappa - 3/2)\, T_{ke} T_{se} + \omega\, (\kappa - 1/2)\, T_{fe} T_{se} + \delta\, (\kappa - 3/2)\, T_{fe} T_{ke}}, \tag{2.3b}$$

where b is the trapped electron coefficient, β is the temperature ratio between the free and trapped electrons, σ_{fe} is the temperature ratio between the free and effective electrons and σ_{te} is the temperature ratio between the trapped and effective

https://doi.org/10.1017/S0022377826101846 Published online by Cambridge University Press

electrons. The investigation of phase-space electron holes, wherein electrons are confined within a localised region, requires that the fraction of trapped electrons remains significantly smaller than the total electron population. This constraint is quantified by the trapped coefficient b, which characterises the degree of electron trapping and dictates how the flattening, depletion or enhancement of the trapped electron distribution influences the effective nonlinearity of the system. In the reductive perturbation expansion we treat the temperature ratios $\beta = T_{fe}/T_{te}$ and σ_O as $O(1)$ and therefore do not expand them in ε. The trapping parameter b originates from the Schamel distribution and quantifies the trapped-population fraction; its ordering is chosen to balance nonlinearities. With the standard Korteweg de Vries (KdV) stretching $\phi \sim \varepsilon$, $\partial_\xi \sim \varepsilon^{1/2}$, $\partial_\tau \sim \varepsilon^{3/2}$, the convective term scales as $\phi\,\phi_\xi = O(\varepsilon^{3/2})$ (Washimi & Taniuti 1966). We therefore order b so that the trapping nonlinearity (e.g. $b\,|\phi|\,\phi_\xi$, or in closures yielding $b\,|\phi|^{1/2}\phi_\xi$ take $b \sim \varepsilon^{1/2}$) enters at the same asymptotic order, producing a Schamel–KdV equation rather than a standard KdV equation (Schamel 1972). If b is ordered smaller, the trapping term drops out at leading order; if larger, the KdV-type balance is lost. Thus, smallness is attributed to the trapped population (b), not to the temperature ratios themselves. On the other hand, the scaling of $b \sim \varepsilon^{1/2}$ is to include both the nonlinear terms, the results from the trapping and the convective term, in the final evolution equation. Otherwise, we obtain a usual KdV equation without incorporating the trapping effect (Das & Tagare 1975; Das 1979; Das *et al*. 1986). Under the assumption of a weak electrostatic potential amplitude, the reductive perturbation technique is applied to the governing hydrodynamic equations, ultimately yielding the Schamel–KdV equation (Schamel 1972).

Observations from multiple spacecraft, including Helios, Ulysses, Cluster II and PSP (Štverák *et al.* 2008; Abraham *et al.* 2022; Shaaban *et al*. 2025), indicate that solar-wind electrons exhibit a dual velocity distribution, consisting of a cool, dense thermal core with number density n_{se} and a hotter, more dilute suprathermal halo with number density n_{ke}. These two populations are well described by a Maxwellian (Boltzmann) distribution for the core,

$$n_{se} = \exp(\phi/\sigma_{se}), \tag{2.4}$$

and a Kappa distribution for the halo,

$$n_{ke} = \left[1 - \frac{\phi/\sigma_{ke}}{(\kappa - 3/2)}\right]^{-\kappa+1/2}, \tag{2.5}$$

respectively (Afify *et al*. 2021), where the total solar-wind electron number density is given by $n_W = n_{se} + n_{ke}$, $\sigma_{se} = T_{se}/T_{eff}$ is the ratio of the solar-wind thermal electron to the effective electron temperatures, $\sigma_{ke} = T_{ke}/T_{eff}$ is the ratio of the solar-wind suprathermal electron to the effective electron temperatures and $\kappa \in [3/2, \infty]$ is the Kappa power index.

The set of equations (2.1)–(2.5) is completed by the Poisson equation:

$$\frac{\partial^2\phi}{\partial x^2} = \mu n_e + \omega n_{ke} + \delta n_{se} - \psi n_{sp} - \alpha n_{H^+} - n_{O^+}, \tag{2.6}$$

where $\mu = n_{te}^{(0)}/n_{O^+}^{(0)}$, $\omega = n_{ke}^{(0)}/n_{O^+}^{(0)}$, $\delta = n_{se}^{(0)}/n_{O^+}^{(0)}$, $\alpha = n_{H^+}^{(0)}/n_{O^+}^{(0)}$ and $\psi = n_{sp}^{(0)}/n_{O^+}^{(0)}$.

It is worth noting that the physical quantities in (2.1)–(2.6), i.e. n_j, u_i, ϕ, x, t, are normalised by using the unperturbed density $n_j^{(0)}$ of the jth species, ion-acoustic

https://doi.org/10.1017/S0022377826101846 Published online by Cambridge University Press

speed $c_{sO^+} = \sqrt{k_B T_{eff}/m_{O^+}}$, the electrostatic potential $k_B T_{eff}/e$, the inverse of the effective Debye length $\lambda_D^{-1} = \sqrt{n_{O^+}^{(0)} e^2/\epsilon_0 k_B T_{eff}}$, the ion plasma frequency $\omega_{pO^+} = \sqrt{n_{O^+}^{(0)} e^2/\epsilon_0 m_{O^+}}$, $\lambda_D/c_{sO^+} = 1/\omega_{pO^+}$, where j refers to plasma species (H^+, O^+, e, sp, ke), i refers to plasma species (H^+, O^+, sp), k_B is the Boltzmann constant and e is the electron charge. Oxygen is the dominant ion in the studied altitude range; therefore, normalisation is based on its acoustic speed and effective Debye length. Under this scheme, waves can appear either subsonic or supersonic, consistent with observations. In comparison, hydrogen-based normalisation yields $U < 1$, making all waves appear subsonic (Sayed *et al*. 2020).

3. The evolution equation

The essential characteristics of small but finite-amplitude IAWs are investigated using the reductive perturbation method (Washimi & Taniuti 1966). We introduce the extended space–time transformation $\xi = \varepsilon^{1/2}(x - \lambda t)$ and $\tau = \varepsilon^{3/2} t$, where λ is the linear phase velocity normalised to c_{sO^+} and ε is a small parameter characterising the smallness of the amplitude or dispersion of the nonlinear modes. The normalised physical quantities n_j, u_i and ϕ are extended around their equilibrium values in the power series of ε as

$$n_j = 1 + \varepsilon n_j^{(1)} + \varepsilon^2 n_j^{(2)} + \varepsilon^3 n_j^{(3)} + \cdots, \tag{3.1a}$$

$$u_i = \varepsilon u_i^{(1)} + \varepsilon^2 u_i^{(2)} + \varepsilon^3 u_i^{(3)} + \cdots, \tag{3.1b}$$

$$u_{sp} = u_{sp}^{(0)} + \varepsilon u_{sp}^{(1)} + \varepsilon^2 u_{sp}^{(2)} + \varepsilon^3 u_{sp}^{(3)} + \cdots, \tag{3.1c}$$

$$\phi = \varepsilon \phi^{(1)} + \varepsilon^2 \phi^{(2)} + \varepsilon^3 \phi^{(3)} + \cdots. \tag{3.1d}$$

Theoretically, IAWs in plasmas are explained by the Schamel–KdV equation, especially when electron trapping is significant. Non-isothermality in this scenario is a description for departures from the isothermality assumption; i.e. the situation in which electron temperature is assumed to be constant. It involves the introduction of a small percentage of non-isothermality to explain small changes in thermal properties occurring due to the existence of both free (Maxwellian) and confined electron species. The Schamel distribution finds application in the case of consideration of electrostatic potentials with small amplitudes. Ion-acoustic waves are generated because of the disturbance of the plasma species around an equilibrium state. These disturbances are mainly generated by the perturbation in number densities, fluid velocities and electrostatic potential. As a result, in our model, we took into account the change of fluid of the plasma species. We take a small percentage of trapped electrons $b = \acute{b}\varepsilon^{1/2}$ and apply the stretching space–time coordinates and expansion equations (3.1) to fluid equations (2.1)–(2.6). The lowest-order equations in ε include (Das *et al*. 1986; El-Labany, El-Warraki & Moslem 2000)

$$u_{O^+}^{(1)} = \frac{\lambda \phi^{(1)}}{\lambda^2 - 3\sigma_{O^+}}, \quad n_{O^+}^{(1)} = \frac{\phi^{(1)}}{\lambda^2 - 3\sigma_{O^+}}, \tag{3.2a}$$

$$u_{H^+}^{(1)} = \frac{\lambda \rho_{H^+} \phi^{(1)}}{\lambda^2 - 3\sigma_{H^+}\rho_{H^+}}, \quad n_H^{(1)} = \frac{\rho_{H^+} \phi^{(1)}}{\lambda^2 - 3\sigma_{H^+}\rho_{H^+}}, \tag{3.2b}$$

https://doi.org/10.1017/S0022377826101846 Published online by Cambridge University Press

$$u_{sp}^{(1)} = \frac{\left(\lambda - u_{sp}^{(0)}\right)\rho_{sp}\phi^{(1)}}{\left(\lambda - u_{sp}^{(0)}\right)^2 - 3\sigma_{sp}\rho_{sp}}, \quad n_{sp}^{(1)} = \frac{\rho_{sp}\phi^{(1)}}{\left(\lambda - u_{sp}^{(0)}\right)^2 - 3\sigma_{sp}\rho_{sp}}, \tag{3.2c}$$

$$n_e^{(1)} = \phi^{(1)}/\sigma_{fe}, \tag{3.2d}$$

$$n_{se}^{(1)} = \phi^{(1)}/\sigma_{se}, \tag{3.2e}$$

$$n_{ke}^{(1)} = \frac{(\kappa - 1/2)}{(\kappa - 3/2)}\frac{\phi^{(1)}}{\sigma_{ke}}. \tag{3.2f}$$

The Poisson equation (2.6) gives the compatibility condition as

$$\frac{\mu}{\sigma_{fe}} + \frac{\omega}{\sigma_{ke}}\left(\frac{\kappa - 1/2}{\kappa - 3/2}\right) + \frac{\delta}{\sigma_{se}} - \frac{\psi\rho_{sp}}{\left(\lambda - u_{sp}^{(0)}\right)^2 - 3\sigma_{sp}\rho_{sp}} - \frac{\alpha\rho_{H^+}}{\lambda^2 - 3\sigma_{H^+}\rho_{H^+}} - \frac{1}{\lambda^2 - 3\sigma_{O^+}} = 0. \tag{3.3}$$

Extending the perturbation expansion to higher orders of ε yields a set of equations that characterise the dynamics of the second-order perturbed quantities. To solve this system, we utilise the framework provided by (3.2), which enables the systematic derivation of the Schamel–KdV equation for electrostatic potential:

$$\frac{\partial\phi}{\partial\tau} + \left[\acute{C}\sqrt{\phi} + \acute{A}\,\phi\right]\frac{\partial\phi}{\partial\xi} + D\frac{\partial^3\phi}{\partial\xi^3} = 0, \tag{3.4}$$

where $\acute{C} = CD$, $\acute{A} = DA$, A and C are the coefficients of the nonlinearity and D is the coefficient of the dispersion, defined as

$$A = \frac{3\psi\rho_{sp}{}^2\left[\left(\lambda - u_{sp}^{(0)}\right)^2 + \sigma_{sp}\rho_{sp}\right]}{\left[\left(\lambda - u_{sp}^{(0)}\right)^2 - 3\sigma_{sp}\rho_{sp}\right]^3} + \frac{3\lambda^2 + 3\sigma_{O^+}}{\left(\lambda^2 - 3\sigma_{O^+}\right)^3} + \alpha\frac{3\lambda^2\rho_{H^+}{}^2 + 3\sigma_{H^+}\rho_{H^+}{}^3}{\left(\lambda^2 - 3\sigma_{H^+}\rho_{H^+}\right)^3} - \frac{\mu}{\sigma_{fe}^2} - \frac{\omega}{\sigma_{ke}^2}\frac{(\kappa - 1/2)\,(\kappa + 1/2)}{(\kappa - 3/2)^2} - \frac{\delta}{\sigma_{se}^2}, \tag{3.5a}$$

$$C = 2\mu\, b\, \sigma_{te}^{-3/2}, \tag{3.5b}$$

$$\frac{1}{D} = \frac{2\left(\lambda - u_{sp}^{(0)}\right)\rho_{sp}\psi}{\left[\left(\lambda - u_{sp}^{(0)}\right)^2 - 3\sigma_{sp}\rho_{sp}\right]^2} + \frac{2\lambda}{\left(\lambda^2 - 3\sigma_{O^+}\right)^2} + \frac{2\lambda\rho_{H^+}\alpha}{\left(\lambda^2 - 3\sigma_{H^+}\rho_{H^+}\right)^2}. \tag{3.5c}$$

The nonlinearity and dispersion in the Schamel–KdV equation play a crucial role in understanding the evolution of IAWs. To obtain the analytical solutions of the Schamel–KdV equation, we use travelling-wave transformation $\eta = \xi - U\tau$ which transforms the nonlinear partial differential equation into an ordinary differential equation in terms of η, corresponding to stationary-wave structures in a frame moving with velocity, where U is the normalised propagation speed of the nonlinear wave in the co-moving frame in which the structure is stationary. This equation is integrated by applying the appropriate boundary condition $\phi(\eta) = \mathrm{d}\phi/\mathrm{d}\eta = \mathrm{d}^2\phi/\mathrm{d}\eta^2 = 0$ at $\eta \to \pm\infty$, from which we get the solitary solution.

https://doi.org/10.1017/S0022377826101846 Published online by Cambridge University Press

Plasma parameter	Value	Plasma parameter	Value
α	0.03	σ_H	0.26
ψ	0.43	σ_{sp}	1.28
ω	0.05	σ_{ke}	2.5
δ	0.43	σ_{se}	1.28
σ_O	0.20	β	0.5
$u_{sp}^{(0)}$	17	κ	5
σ_{te}	5	σ_{fe}	1.03
U	0.5		

TABLE 1. Plasma parameters used in the SW analysis.

The electrostatic potential due to the localised solitary solution of (3.4) is given by (Tagare & Chakrabarti 1974; Das 1979; Dönmez & Dağhan 2017)

$$\phi_s = \left[\frac{4CD}{15U} + \sqrt{\frac{16C^2D^2}{225U^2} + \frac{AD}{3U}}\cosh\left(\sqrt{\frac{U}{4D}}\,\eta\right)\right]^{-2}. \tag{3.6}$$

The electric field E_s associated with SWs from (3.6) is given by

$$E_s = -\frac{\sqrt{U/D}\sqrt{(AD/3U) + (16C^2D^2/225U^2)}\sinh\left((1/2)\eta\sqrt{U/D}\right)}{\left[\sqrt{(AD/3U) + 16C^2D^2/225U^2}\cosh\left((1/2)\eta\sqrt{U/D}\right) + 4CD/15U\right]^3}. \tag{3.7}$$

When we apply the appropriate boundary conditions $V(\phi) = \mathrm{d}V/\mathrm{d}\phi = 0$, $\mathrm{d}V^2/\mathrm{d}^2\phi < 0$ at $\phi = \phi_{max} = 4C^2A^{-2}/25$, we will get the DLs. The electrostatic potential due to the DL solution of (3.4) is given by (Das 1979; Das *et al*. 1986; Dönmez & Dağhan 2017; Soliman, Zahran & Elkamash 2023)

$$\phi_D = \frac{4C^2}{25A^2}\left[1 - \tanh\left(\eta\sqrt{\frac{U}{16D}}\right)\right]^2. \tag{3.8}$$

The corresponding electric field E_D reads

$$E_D = -\frac{2\sqrt{U}C^2}{25\sqrt{D}A^2}\left[1 - \tanh\left(\eta\sqrt{\frac{U}{16D}}\right)\right]\mathrm{sech}^2\left(\eta\sqrt{\frac{U}{16D}}\right). \tag{3.9}$$

4. Numerical analysis and discussion

In this section, we investigate the propagation characteristics of IAWs at the upper mantle boundary of Venus and compare them with observed electrostatic structures. The analysis is conducted using plasma parameters adopted from *in situ* measurements by the VEX spacecraft (Lundin *et al*. 2011; Knudsen *et al*. 2016). The relevant plasma parameters are summarised in tables 1–3, covering SW (table 1) and DL (table 2) cases, as well as the observed plasma parameters, their corresponding normalised quantities and their effects on the electrostatic solutions (table 3). We

https://doi.org/10.1017/S0022377826101846 Published online by Cambridge University Press

Plasma parameter	Value	Plasma parameter	Value
α	0.28	σ_H	0.01
ψ	0.16	σ_{sp}	2
ω	0.016	σ_{ke}	2.5
δ	0.3	σ_{se}	1.67
σ_O	0.04	β	0.4
$u_{sp}^{(0)}$	15	κ	5
σ_{te}	5	σ_{fe}	1.25
U	0.2		

TABLE 2. Plasma parameters used in the DL analysis.

Parameter	Observed	Norm. parameter	Value	Effect
n_{O^+} (cm^{-3})	5–60	—	—	—
$n_{H^+}^{(0)}$ (cm^{-3})	2–20	$\alpha = n_H^{(0)}/n_{O^+}^{(0)}$	0.03−0.5	SW(+) – DL(+)
$n_{sp}^{(0)}$ (cm^{-3})	10–17	$\psi = n_{sp}^{(0)}/n_{O^+}^{(0)}$	0.16−0.43	SW(−) – DL(−)
$n_{ke}^{(0)}$ (cm^{-3})	1–5	$\omega = n_{ke}^{(0)}/n_O^{(0)}$	0.016−0.1	SW(N) – DL(−)
$n_{se}^{(0)}$ (cm^{-3})	10–17	$\delta = n_{se}^{(0)}/n_{O^+}^{(0)}$	0.16−0.43	SW(N) – DL(−)
T_{H^+} (eV)	1–2	$\sigma_H = T_{H^+}/T_{eff}$	0.1−0.26	SW(−) – DL(−)
T_{O^+} (eV)	1–2	$\sigma_O = T_{O^+}/T_{eff}$	0.1−0.2	SW(N) – DL(−)
T_{sp} (eV)	10–20	$\sigma_{sp} = T_{sp}/T_{eff}$	1.28−2.6	SW(N) – DL(−)
T_{se} (eV)	10–30	$\sigma_{se} = T_{se}/T_{eff}$	1.28−4	SW(+) – DL(+)
T_{fe} (eV)	8–12	$\sigma_{fe} = T_{fe}/T_{eff}$	1−1.67	SW(+) – DL(−)
T_{ke} (eV)	20–50	$\sigma_{ke} = T_{ke}/T_{eff}$	2.5−6.67	SW(N) – DL(−)
T_{te} (eV)	20–50	$\sigma_{te} = T_{te}/T_{eff}$	2.5−6.67	SW(N) – DL(+)
u_{sp} (km s^{-1})	80–120	$u_{sp}^{(0)} = u_{sp}/c_{sO^+}$	13−17	SW(−) – DL(−)
—	—	κ	1.5−10	SW(+) – DL(−)
—	—	$\beta = T_{fe}/T_{te}$	0.2−0.5	SW(N) – DL(−)

TABLE 3. The observed and normalised (norm.) values of plasma parameters obtained from VEX missions in the Venus ionosphere (Lundin *et al*. 2011; Knudsen *et al*. 2016) and their effects on the electrostatic waves.

note that the adopted value $\kappa = 5$ is consistent with *in situ* solar-wind observations. The Kappa index decreases with heliocentric distance, with electron distributions approaching Maxwellian conditions (large κ) closer to the Sun and exhibiting stronger suprathermal tails (smaller κ) farther out. Typical inner heliospheric values lie in the range $\kappa \sim 3-7$ (e.g. Maksimovic *et al*. (2005), Lazar *et al*. (2020)), with values near the Venus orbit (∼0.72 AU) typically $\kappa \approx 4-6$.

We analyse two types of nonlinear electrostatic structures, namely SWs and DLs. Using the compatibility condition given in (3.3), we identify six distinct roots, each corresponding to a separate phase-velocity mode, denoted by λ. The existence of multiple distinct roots implies the presence of multiple propagation modes, each associated with a specific species or interaction dynamic in the plasma. In figure 1,

https://doi.org/10.1017/S0022377826101846 Published online by Cambridge University Press

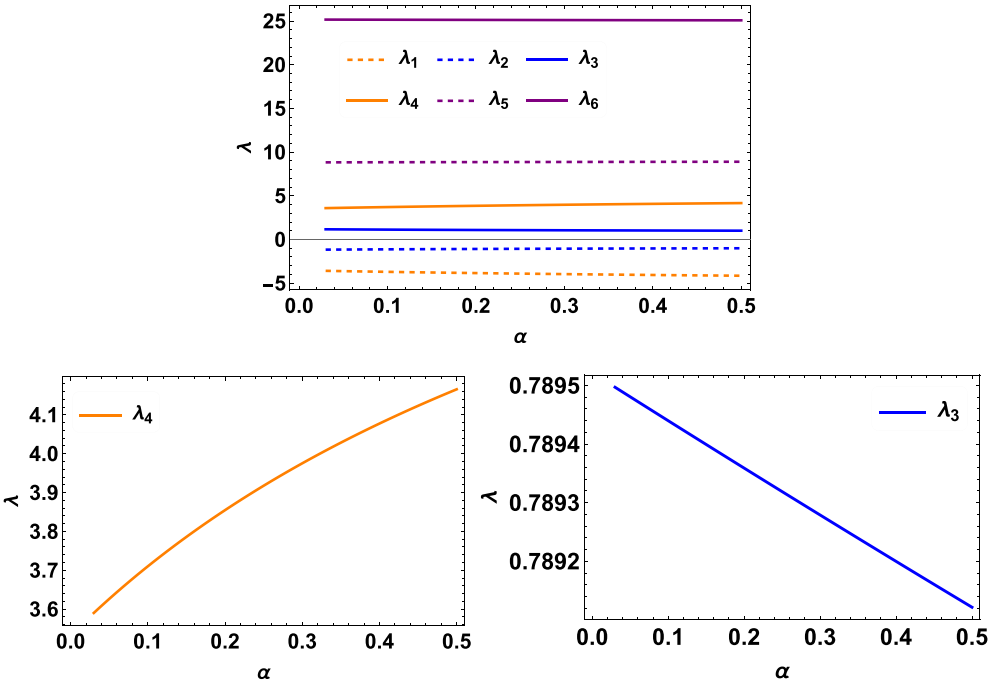


FIGURE 1. Variation of the phase velocities λ_1, λ_2, λ_3, λ_4, λ_5 and λ_6 with the hydrogen density ratio α. Other plasma parameters are $\psi = 0.43$, $\omega = 0.05$, $\delta = 0.43$, $\sigma_{sp} = 1.28$, $\sigma_H = 0.26$, $\sigma_O = 0.2$, $\sigma_{se} = 1.28$, $\sigma_{ke} = 2.5$, $\sigma_{fe} = 1.03$, $\sigma_{te} = 5$, $\beta = 0.5$, $u_{sp}^{(0)} = 17$ and $\kappa = 5$.

we examine the variation of the phase velocities, represented by the roots λ_{1-6}, as functions of the hydrogen density ratio α (top panel). Among the six modes, four are forward-propagating ($\lambda > 0$), labelled as λ_3 to λ_6, and two are backward-propagating ($\lambda < 0$), labelled as λ_1 and λ_2. The classification of these modes is based on the mass and initial velocity of the plasma species involved. The faster modes correspond to lighter species, whereas the slower modes correspond to heavier species. Accordingly, λ_2 and λ_3 are attributed to planetary oxygen ions, λ_1 and λ_4 to planetary hydrogen ions and λ_5 and λ_6 to solar-wind protons. Notably, both oxygen and hydrogen ions exhibit forward and backward modes. The bottom panels of figure 1 illustrate the variation of phase velocities for oxygen (λ_3) and hydrogen (λ_4) ions with respect to α. It is observed that the phase velocity λ_4 associated with hydrogen ions increases slightly as α increases, whereas the phase velocity λ_3 corresponding to oxygen ions exhibits no significant change with α. Here, the phase velocity is obtained from the linear dispersion relation (3.3), which governs small-amplitude perturbations around the equilibrium state. At this level, α does not influence the restoring forces; therefore, the phase velocity is expected to be independent of α.

The presence of streaming solar-wind protons with initial velocity $u_{sp}^{(0)}$ induces a Doppler shift in the phase-velocity mode λ_5 (dashed purple line in figure 1), effectively displacing it from its intrinsic backward-propagating regime into the forward region when viewed in the oxygen plasma frame. Although λ_5 remains negative in its rest frame, it appears as a forward-propagating mode due to this transformation. In contrast, λ_6 (solid purple line) intrinsically exceeds $u_{sp}^{(0)}$, affirming its presence in the forward regime. Motivated by the observations of electrostatic structures in the

https://doi.org/10.1017/S0022377826101846 Published online by Cambridge University Press

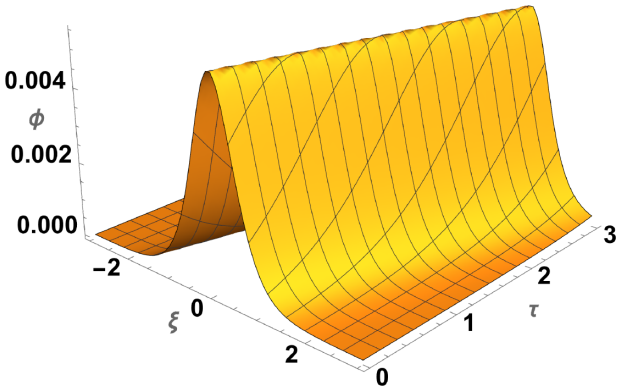


FIGURE 2. The electrostatic potential ϕ of the SW as a function of ξ and τ. The plasma parameters are tabulated in table 1.

Venusian plasma environment, we now focus on the modes that correspond to these features. The fourth root, λ_4 (solid orange line), is associated with SW structures, while the third root, λ_3 (solid blue line), is linked to the generation of DLs. The variation and characteristics of these two modes are discussed in detail in the following sections.

4.1. *Solitary wave*

In this section, we perform a comprehensive parametric analysis to investigate the characteristics of solitary structures by examining the electrostatic potential (ϕ), associated electric field (E), characteristic time scale (T), observed frequency (f) and power spectral features, as functions of key plasma parameters. Table 1 provides a summary of the plasma parameters that were used in our numerical study of the SW, unless otherwise specified.

Figure 2 illustrates the electrostatic potential of a SW as a function of ξ and τ in three dimensions. The three-dimensional representation is used to provide a comprehensive view of the potential structure and its spatial–temporal variation. Since a soliton (or SW) maintains a fixed shape during propagation, its potential profile is more effectively analysed using the single combined variable η within the same wave frame, as shown in the subsequent figures.

In figure 3, we present the variation of the electrostatic potential ϕ as a function of the normalised distance η for different plasma parameters. The top-left panel illustrates the influence of the hydrogen-to-oxygen density ratio α, while the top-right panel shows the effect of the solar wind proton-to-oxygen density ratio ψ. The middle-left panel displays the dependence on the streaming velocity of solar-wind protons u_{sp} and the middle-right panel highlights the role of the suprathermal electrons through the Kappa index κ. Finally, the bottom-left panel demonstrates the variation with the ratio of the solar-wind thermal electron temperature to the effective temperature, σ_{se}, whereas the bottom-right panel depicts the effect of the trapped non-isothermal ionospheric electron temperature ratio σ_{fe}.

An increase in the hydrogen density ratio α enhances the amplitude ϕ of the SW, as illustrated by the blue curve for $\alpha = n_H/n_O = 0.05$. One possible explanation is that an increase in the hydrogen density enhances the population of hydrogen ions with higher phase velocities and thermal energies, thereby introducing additional free

https://doi.org/10.1017/S0022377826101846 Published online by Cambridge University Press

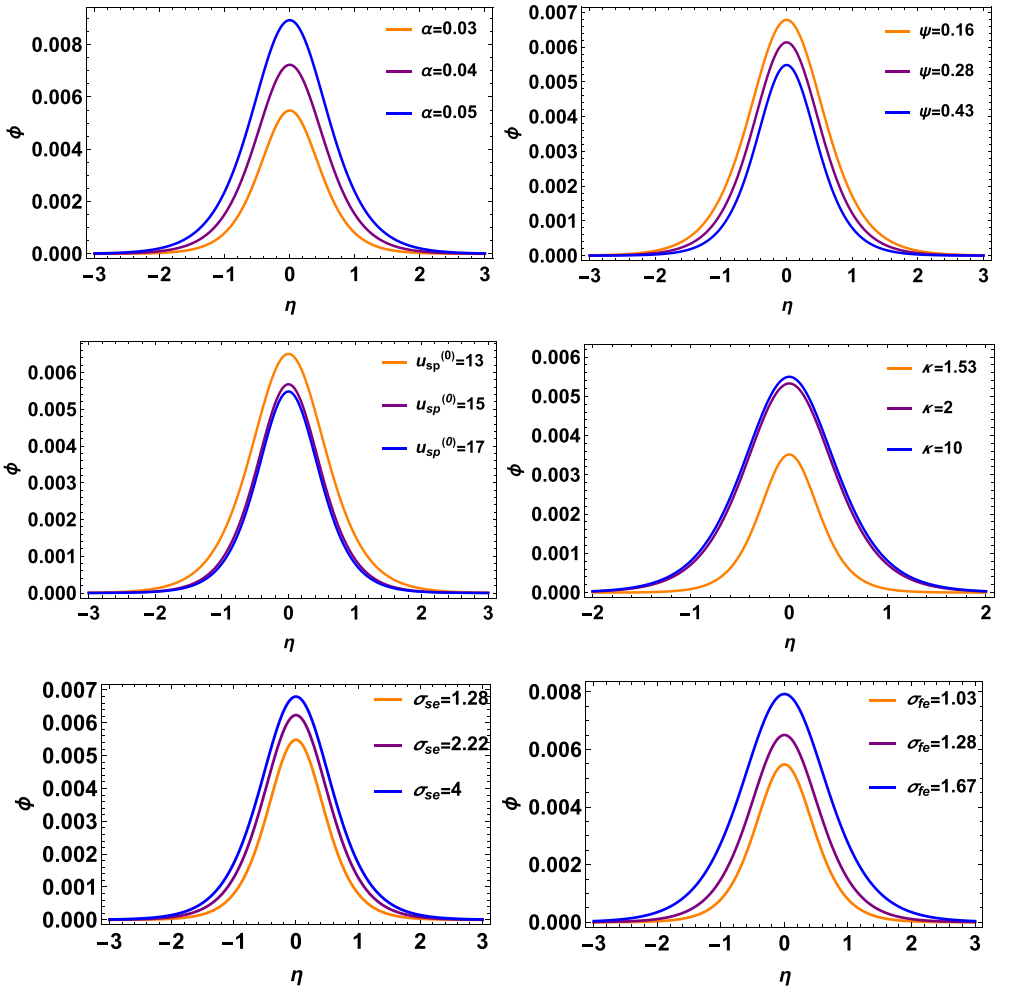


FIGURE 3. Variation of the electrostatic potential (amplitude) ϕ of the SW as a function of η for different plasma parameters: $\alpha = 0.03, 0.04, 0.05$ (top left), $\psi = 0.16, 0.28, 0.43$ (top right), $u_{sp} = 13, 15, 17$ (middle left), $\kappa = 1.53, 2, 10$ (middle right), $\sigma_{se} = 1.28, 2.22, 4$ (bottom left), $\sigma_{fe} = 1.03, 1.28, 1.67$ (bottom right). Other plasma parameters are tabulated in table 1.

energy into the system. Consequently, the ion-acoustic speed is increased, which in turn leads to an amplification of the electrostatic potential. In contrast to the linear case shown in figure 1, where the phase velocity remains essentially unaffected by α, the nonlinear regime exhibits a pronounced dependence. Within Sagdeev's pseudopotential framework, α explicitly modifies the nonlinear coefficients, significantly influencing the amplitude and profile of SWs discussed here and DLs addressed in the following section. The solar-wind protons exert inhibiting effects on the electrostatic SW; the amplitude ϕ decreases with increasing density n_{sp} or the flow velocity u_{sp} of the solar-wind protons, as shown in the top-right and middle-left panels, respectively. An increase in the velocity of the streaming solar protons causes the ions to move faster, thereby reducing the net energy exchange between ions and the plasma environment. This reduction in energy transfer ultimately leads to a decrease in the electrostatic potential.

https://doi.org/10.1017/S0022377826101846 Published online by Cambridge University Press

On the other hand, solar-wind and ionospheric electrons exhibit a stimulating effect on the SW; the amplitude ϕ increases with increasing electron temperatures T_{se} and T_{fe} relative to the effective plasma temperature, as shown in the bottom-left and bottom-right panels, respectively. In contrast, the κ-distributed solar-wind electrons display an opposite behaviour, with ϕ decreasing as κ decreases, i.e. as the suprathermal population increases. This trend is illustrated by the orange curve for $\kappa = 1.53$ in the middle-right panel. This behaviour can be explained as follows: lowering κ enhances the population of suprathermal electrons, which become more energetic and are more likely to escape, carrying away a significant fraction of the system's energy. Consequently, both the charge balance and the effective energy exchange between the remaining electrons and ions are reduced, leading to a decrease in the electrostatic potential amplitude. The effects of all plasma parameters in our plasma system are summarised in table 3.

In figure 4, we examine the characteristics of electrostatic SWs, which exhibit a bipolar pulse structure similar to those observed by PVO in the Venus mantle environment (Scarf *et al.* 1980*b*; Hadid *et al*. 2021), for selected plasma parameters from figure 3, namely α (top row), ψ (second row), κ (third row) and σ_{se} (bottom row). The left-hand column shows the temporal profiles of the electric field (in $\mathrm{mV\,m^{-1}}$) as a function of time T (in s), while the right-hand column displays the corresponding power spectra dB (in $\mathrm{mV\,m^{-1}/\sqrt{Hz}}$) as a function of the logarithmic frequency $\log_{10}(\nu\ [\mathrm{Hz}])$, computed using the fast Fourier transform (FFT) of the bipolar pulse. The FFT method is particularly suited for analysing signals with periodic or recurrent patterns in time or space, as it decomposes the signal into sinusoidal components (Kakad, Kakad & Omura 2014; Salem *et al*. 2022). From this decomposition, the dominant frequency components of a solitary pulse can be extracted, providing the characteristic frequency of the solitary structure (Salem *et al*. 2022; Morsi *et al*. 2024; Gamal *et al*. 2025). These frequencies can then be compared with theoretical predictions for IAWs and with observational data, thereby confirming the validity of our model.

In the left-hand panels, both the amplitude of the electric field and the duration of the bipolar pulse increase with higher hydrogen densities (i.e. increasing α) and solar-wind electron temperatures (i.e. increasing σ_{se}), while they decrease with higher solar-wind proton densities (i.e. increasing ψ) and enhanced suprathermal populations of solar-wind electrons (i.e. decreasing κ), consistent with the results shown in figure 3. The corresponding FFT power spectra of the electric field are shown in the right-hand panels of figure 4. Within these spectra, the peak frequency corresponds to the single frequency at which the FFT spectrum of the bipolar electric field reaches its maximum, indicating the strongest oscillation or dominant wave mode. In contrast, the dominant frequency captures the broader range of significant frequencies contributing the majority of spectral power, representing the cumulative energy that influences plasma dynamics. The peak frequencies appear at 500, 524 and 549 Hz for $\alpha = 0.05$, 0.04 and 0.03, respectively (top row); at 501, 513 and 540 Hz for $\psi = 0.43$, 0.28 and 0.16, respectively (second row); at 560, 560 and 575 Hz for $\kappa = 10$, 2 and 1.53, respectively (third row); and at 510, 510 and 525 Hz for $\sigma_{se} = 4$, 2.22 and 1.28, respectively (bottom row). The dominant frequency contributions lie within the ranges $\sim$(400 Hz−3.16 kHz), $\sim$(400 Hz−3.5 kHz) and $\sim$(400 Hz−4 kHz) for $\alpha = 0.05$, 0.04 and 0.03, respectively (top row); within $\sim$(400 Hz−4 kHz), $\sim$(400 Hz−3.5 kHz) and $\sim$(400 Hz−3 kHz) for $\psi = 0.43$, 0.028 and 0.16, respectively (second row); within $\sim$(400 Hz−3.16 kHz), $\sim$(400 Hz−3.2 kHz) and $\sim$(380 Hz−6 kHz) for $\kappa = 10$, 2 and 1.53, respectively (third row);

https://doi.org/10.1017/S0022377826101846 Published online by Cambridge University Press

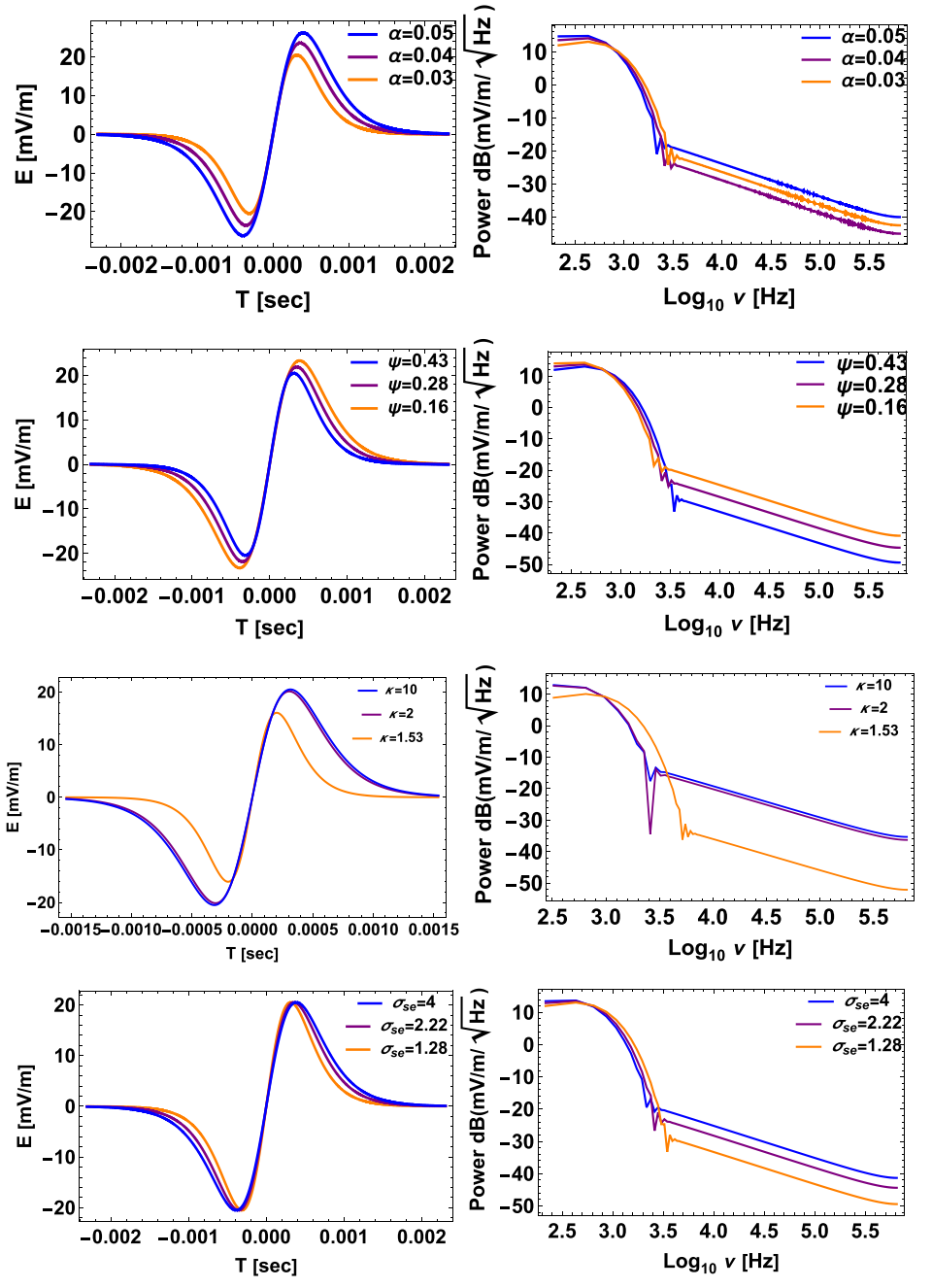


FIGURE 4. Variations of the electric field E as a function of T (left-hand column) and the power spectra as a function $\log_{10}\nu$ (right-hand column) for different plasma parameters: $\alpha = 0.03, 0.04, 0.05$ (top row), $\psi = 0.16, 0.28, 0.43$ (second row), $\sigma_{se} = 1.28, 2.22, 4$ (third row), $\kappa = 1.53, 2, 10$ (bottom row). Other plasma parameters are tabulated in table 1.

and within $\sim$(400 Hz−3 kHz), $\sim$(400 Hz−3.2 kHz) and $\sim$(400 Hz−4 kHz) for $\sigma_{se} = 4$, 2.22 and 1.28, respectively (bottom row).

At this stage, we conclude that our theoretical predictions for the electric field amplitude, $E \sim 20$ mV m^{-1}, the bipolar pulse duration, $T = (2.5-4)$ ms, and the

https://doi.org/10.1017/S0022377826101846 Published online by Cambridge University Press

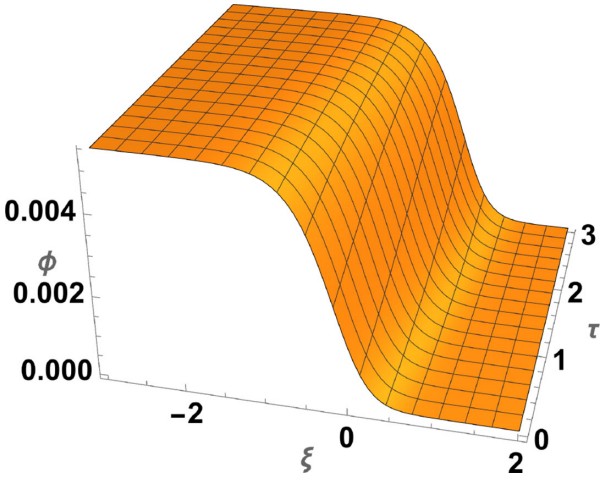


FIGURE 5. The electrostatic potential of the DL structure ϕ, as a function of ξ and τ. Other plasma parameters are tabulated in table 2.

frequency range, $f = 400$ Hz$-$5.6 kHz, are in good agreement with PVO observations, which reported $E \sim 20$ mV m^{-1} and a Doppler-shifted frequency of 5.4 kHz (with a bandwidth of $\pm 15\,\%$ around the central frequency) (Scarf *et al.* 1980*a*; Hadid *et al*. 2021; Rubia *et al*. 2023). This agreement provides strong support for our model of the phase-space electron hole as an electrostatic phenomenon. Furthermore, our results suggest that IAWs can occur at frequencies consistent with those measured by the OEFD, implying that the mantle waves observed in the 5.4 kHz channels can be interpreted as IAWs (Scarf *et al*. 1979; Malaspina *et al*. 2014).

4.2. *Double-layer*

In this section, we perform a parametric analysis of the DL or shock-like nonlinear structure, described by the solution (3.8), to investigate the influence of various plasma parameters on its characteristics, namely the electrostatic potential ϕ, electric field E, time pulse τ, frequency f and power spectrum dB. Unless otherwise specified, the plasma parameters used in our numerical study are summarised in table 2.

To gain a comprehensive view of the potential structure, figure 5 illustrates the three-dimensional variation of the electrostatic potential associated with DLs as a function of the independent variables ξ and τ. Although this three-dimensional representation provides valuable insight, the behaviour is more clearly interpreted using the combined variable η within the same wave frame, as shown in the subsequent figures.

In our analysis of the DLs, we found that the solutions are strongly influenced by the chosen values of α. In particular, there exists a critical (turning point) value at $\alpha \sim 0.28$, where the electrostatic potential undergoes a dramatic change, producing a sharp, thin spike; see the top-left panel of figure 6. Consequently, the overall behaviour and dynamics of the system are significantly altered, as shown in the top-right panel, where the electrostatic potential undergoes a dramatic change within the narrow range $\alpha \in [0.275, 0.285]$; see the inset in the top-left panel. One possible explanation is that the electrostatic potential amplitude is governed by the nonlinear

https://doi.org/10.1017/S0022377826101846 Published online by Cambridge University Press

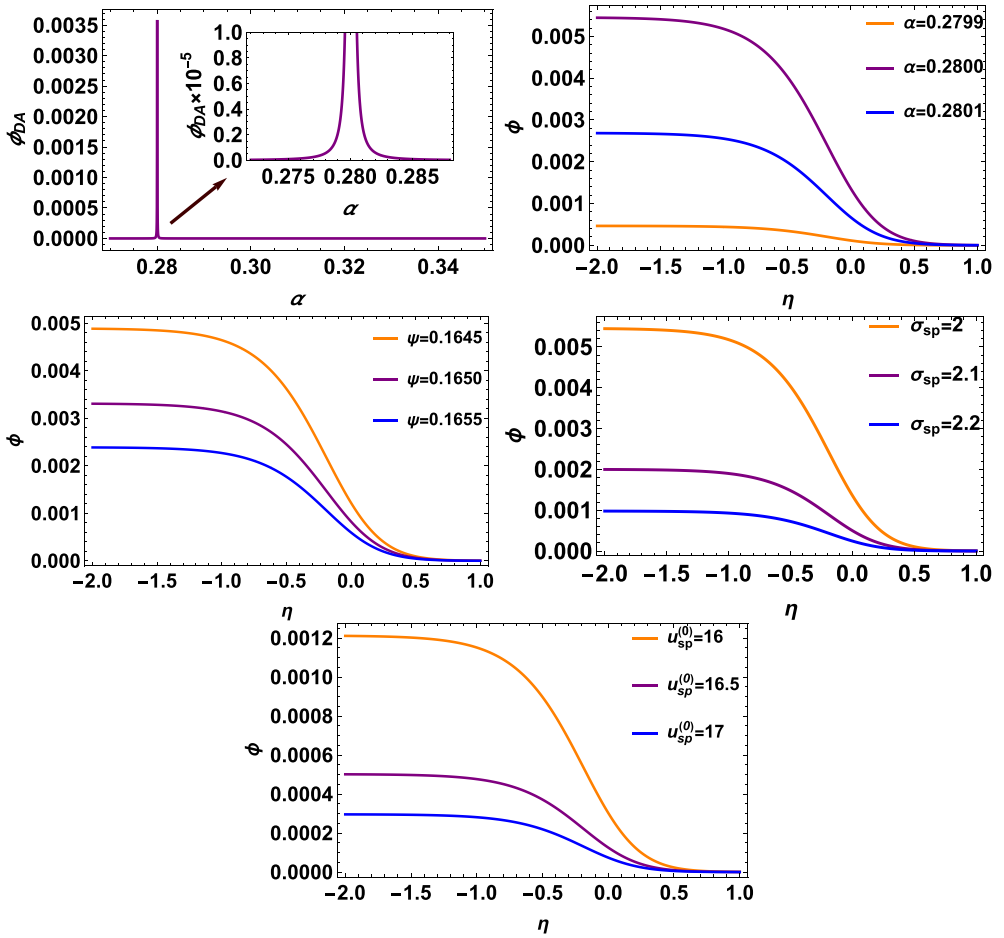


FIGURE 6. Variation of the electrostatic potential of the DL structure ϕ with the ion plasma parameters α (top left), ψ (top right), σ_{sp} (middle left) and $u_{sp}^{(0)}$ (middle right). The DL amplitude $\phi_{DA} = 4C^2A^{-2}/25$ as a function of α (bottom). Other plasma parameters are tabulated in table 2.

coefficient A', which introduces a turning point in the DL behaviour. For α values below this point, increasing α enhances the amplitude, consistent with the SW trend. Beyond the turning point, the amplitude decreases as the sign and contribution of A' change, indicating a shift in the dispersion–nonlinearity balance that controls DL stability. This justifies the use of several significant figures for the value of α in the DL analysis. In the remaining panels of figure 6, we examine the effects of the solar-wind proton parameters on the electrostatic potential ϕ: ψ (middle left), σ_{sp} (middle right) and $u_{sp}^{(0)}$ (bottom). All solar-wind proton parameters exhibit inhibiting effects on the DL solutions. In particular, the electrostatic potential ϕ decreases markedly with increasing solar-wind proton density (increasing ψ), proton temperature (increasing σ_{sp}) and streaming velocity $u_{sp}^{(0)}$. A similar behaviour is observed for the SWs, although with reduced effectiveness, as illustrated in the top-right panel of figure 3. Increasing the solar-wind proton density $n_{sp}^{(0)}$ shortens the effective Debye length, which strengthens electrostatic shielding. For fixed plasma parameters, this

https://doi.org/10.1017/S0022377826101846 Published online by Cambridge University Press

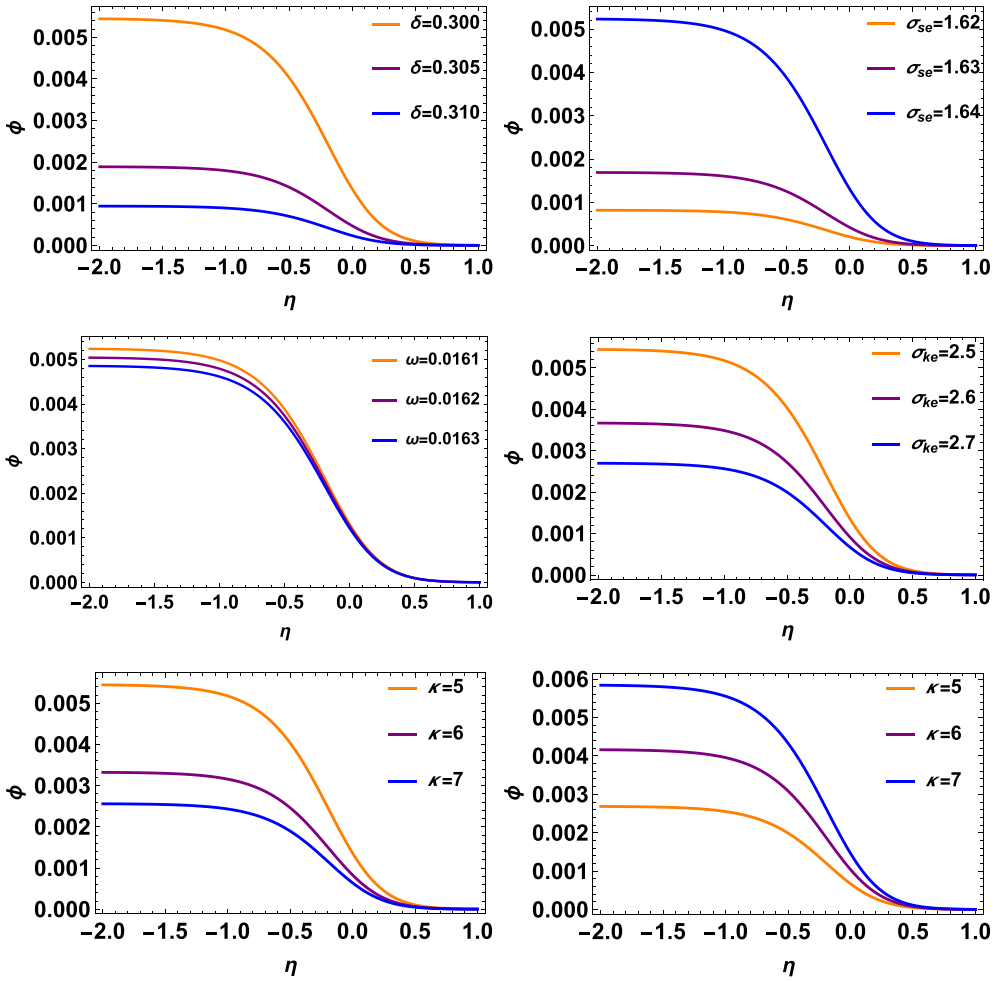


FIGURE 7. Variation of the electrostatic potential of the DL structure ϕ with the electron plasma parameters δ (top left), σ_{se} (top right), ω (middle left) and $\sigma_{\kappa e}$ (middle right). Kappa index κ at $\alpha = 0.2800$ (bottom left) and at $\alpha = 0.2801$ (bottom right). Other plasma parameters are tabulated in table 2.

reduces the net charge separation and lowers the amplitude of the electrostatic potential. Raising the proton temperature increases thermal pressure and the ion velocity, which weakens the nonlinear response, so amplitude decreases. Increasing the solar-wind proton streaming velocity $u_{sp}^{(0)}$ moves the system away from resonance with the IAW phase speed. Near resonance, ions can efficiently exchange energy with the wave, which supports larger amplitudes. As $u_{sp}^{(0)}$ increases beyond this range, the coupling becomes weaker and less energy is transferred into the wave, so the amplitude of the electrostatic potential decreases.

Figure 7 illustrates the influence of various solar-wind electron parameters on the electrostatic potential ϕ, namely δ (top left), σ_{se} (top right), ω (middle left), σ_{ke} (middle right) and κ (bottom). Increasing the density of the thermal (Maxwellian) solar-wind electrons δ introduces a larger population of low-energy electrons. This leads to a redistribution of the electron energy, reducing the net energy of the system.

https://doi.org/10.1017/S0022377826101846 Published online by Cambridge University Press

Consequently, the separation energy between ions and electrons decreases, resulting in a reduction of the electrostatic potential amplitude ϕ, as shown in the top-left panel. However, by increasing the temperature of the solar-wind thermal electrons (increasing σ_{se}), the overall electron energy increases. This enhances the phase velocity of the electrons and, consequently, leads to an increase in the electrostatic potential amplitude ϕ. A similar behaviour is observed for the SWs as illustrated in the bottom-left panel of figure 3. Lowering κ (bottom panel), which increases the fraction of suprathermal solar-wind electrons, introduces more energetic electrons into the system. However, the impact of κ on the DL structure is governed by a critical parameter – the turning point – that acts as a switch, determining the system's response. When α is below this turning point, the electrostatic potential amplitude increases (bottom-left panel), a behaviour opposite to that observed for SWs in the middle-right panel of figure 3. Once α exceeds the turning point, the response aligns with the SW case, resulting in a decrease in the electrostatic potential amplitude (bottom-right panel). A similar effect is observed for the influence of suprathermal populations on plasma structures even at the microscopic level, such as in kinetic plasma instabilities; see the detailed discussion in Lazar (2012) and Shaaban *et al*. (2020).

Figures 8 and 9 present the solutions of the unipolar electrostatic SWs, also referred to as DL structures (Goodrich *et al.* 2018; Morsi *et al*. 2024), obtained for selected ion and electron plasma parameters from figures 6 and 7, respectively. In both figures, the left-hand panels illustrate the time evolution of the electric field (in $\mathrm{mV\,m^{-1}}$), while the right-hand panels show the corresponding power spectra dB (in $\mathrm{mV\,m^{-1}/\sqrt{Hz}}$) as a function of $\log_{10}(\nu\ [\mathrm{Hz}])$, calculated via FFT of the unipolar field structures displayed in the left-hand panels. In all cases, the maximum amplitude of the electric field pulse $E \approx 18\,\mathrm{mV\,m^{-1}}$ is reached within the time interval $T \in [-0.003, 0.0015]$ s, i.e. within a time duration of 4.5 ms. For the ion parameters, the top panels of figure 8 show that the amplitude of the electrostatic potential ϕ and the corresponding FFT power spectra obtained at the critical value $\alpha = 0.28$ are the largest among all considered values of α. Furthermore, the power spectrum is shifted towards higher frequencies. In this case, the dominant frequency contributions are found in the range $\sim$(400 Hz−1.3 kHz), depending on the specific value of α. The solar-wind proton parameters, namely the density ψ (middle panels) and temperature σ_{sp} (bottom panels), exhibit an inhibiting effect on the amplitudes of both ϕ and $\mathrm{d}B$. Increasing either ψ or σ_{sp} leads to a reduction in the amplitudes of ϕ and $\mathrm{d}B$. Moreover, the power spectra are shifted towards lower frequencies, with the dominant frequency contributions lying in the range $\sim$(400 Hz−1.5 kHz) for the different values of ψ and σ_{sp}. The effects of the different plasma parameters on the results presented in figure 8 are consistent with the corresponding behaviours observed in figure 7.

On the other hand, the effects of the solar-wind electron parameters on ϕ and $\mathrm{d}B$ are illustrated in figure 9. In the top panels, increasing the density of thermal electrons leads to a reduction in both the electric field amplitude and the power spectra, with the spectral curves shifted towards lower frequencies. The dominant frequency contributions in this case lie within $\sim$(400 Hz−1.5 kHz) for different values of δ. By contrast, increasing the temperature of the thermal electrons enhances both the electric field and the power spectra amplitudes, while shifting the spectral curves to higher frequencies. The dominant contributions are then located within $\sim$(400 Hz−1.6 kHz) for different values of σ_{se}, as shown in the second row. Furthermore, increasing the temperature of the suprathermal electrons, as well as

https://doi.org/10.1017/S0022377826101846 Published online by Cambridge University Press

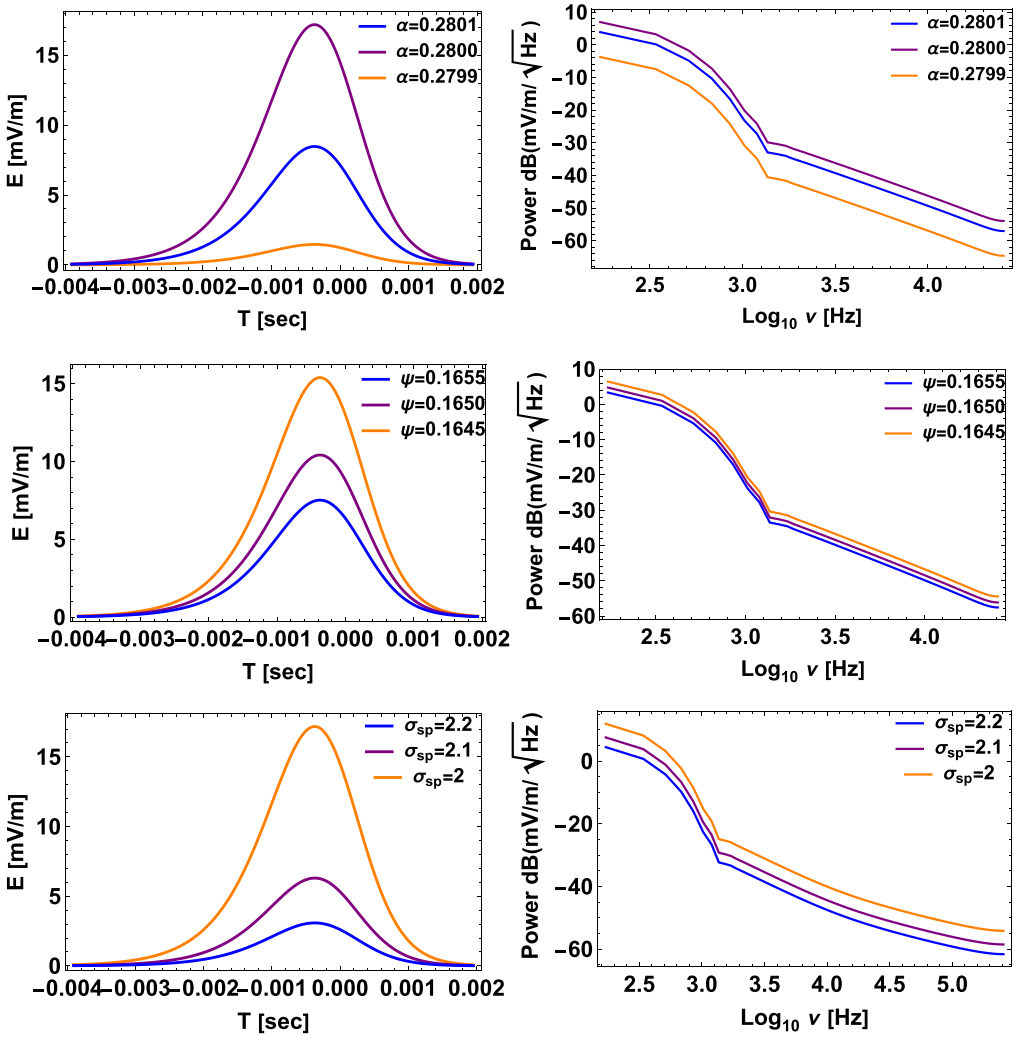


FIGURE 8. Variations of the electric field E (in mV m^{-1}) as a function of time T (in s) (left panels) and the corresponding power spectra in dB [mV m$^{-1}/\sqrt{\text{Hz}}$] as a function of $\log_{10}(\nu$ [Hz]) (right panels) for selected ion plasma parameters from figure 6: α (top), ψ (middle), and σ_{sp} (bottom).

the power index κ of their distribution, results in a decrease of both the electric field and the power spectra amplitudes, accompanied by a shift of the curves towards lower frequencies. The dominant frequency contributions in these cases are within $\sim$(400 Hz$-$1.6 kHz) for varying values of σ_{ke} and κ, as illustrated in the third and bottom rows, respectively.

From these results, we conclude that the FFT of the unipolar DL electric pulse exhibits a broadband electrostatic spectrum, spanning frequencies approximately in the range $\sim$0.4–1.6 kHz, which falls within the broader range of frequencies reported by observations (0.63–5.6 kHz) (e.g. Malaspina *et al*. 2020; Hadid *et al*. 2021). The effects of all plasma parameters considered in this study, including those not explicitly discussed, on both SW and DL solutions are summarised in table 3.

https://doi.org/10.1017/S0022377826101846 Published online by Cambridge University Press

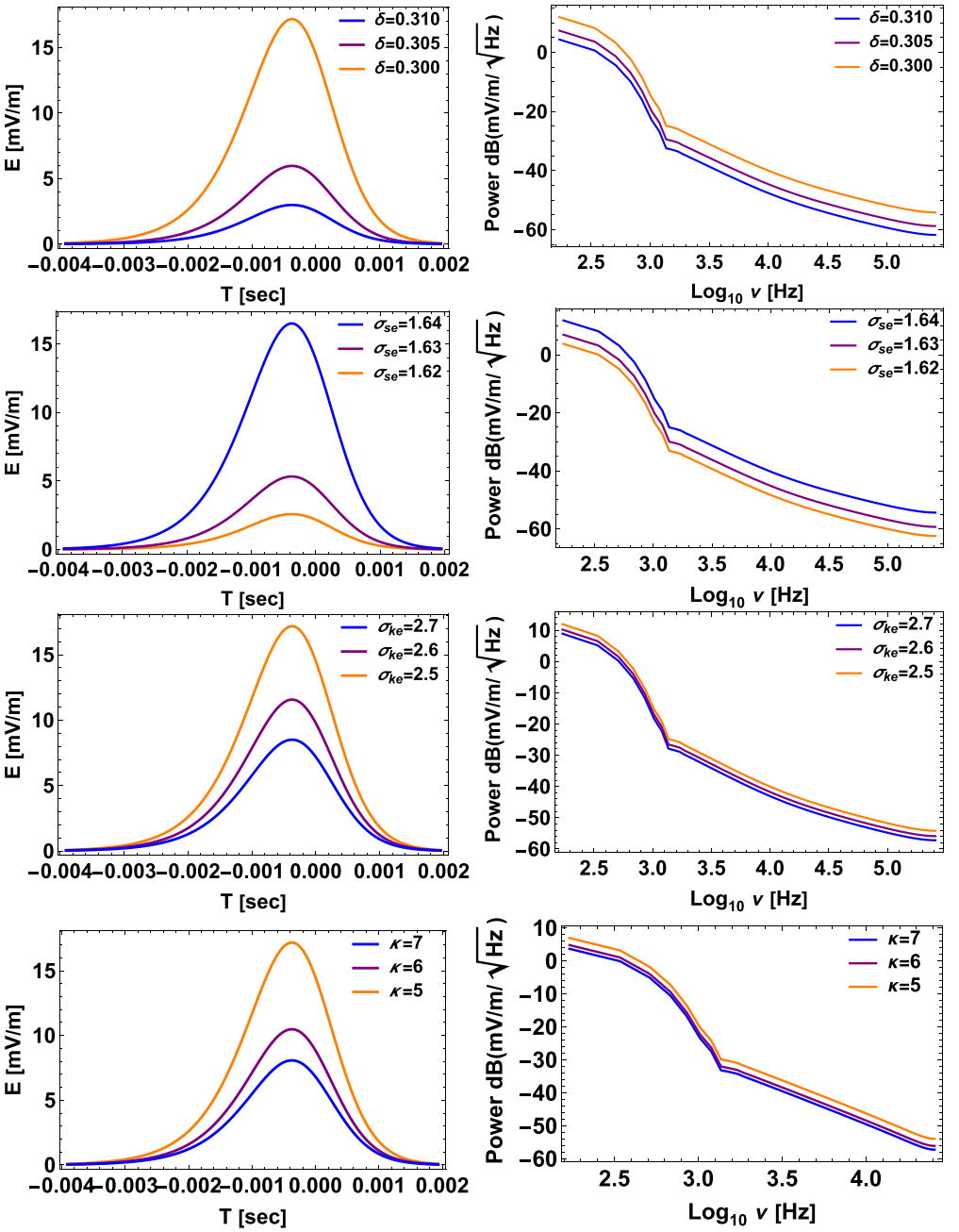


FIGURE 9. Variations of the electric field E as a function of time T (left-hand column) and the corresponding power spectra as a function of $\log_{10}\nu$ (right-hand column) for selected electron plasma parameters from figure 7: δ (top row), σ_{se} (second row), $\sigma_{\kappa e}$ (third row) and κ (bottom row).

In this table, the symbols '+' and '−' indicate that a given plasma parameter has a stimulating or inhibiting effect, respectively, on the studied electrostatic wave structures. The letter 'N' denotes a negligible effect.

https://doi.org/10.1017/S0022377826101846 Published online by Cambridge University Press

Physical quantity	DLs	SWs	Observations
Potential (V)	0.001−0.0012	0.003−0.009	—
Electric field (mV m^{-1})	∼18	∼20	∼15
Pulse duration (ms)	∼4.5	∼3	∼0.6
FFT frequency (kHz)	∼0.7−1.6	∼0.4−6	∼5.6

TABLE 4. Summary of the observed plasma parameters in the Venus ionosphere, based on VEX mission observations (Hadid *et al*. 2021; Scarf *et al*. 1980*a*), compared with our theoretical results for SWs and DLs.

5. Conclusion

In this work, we employed a fluid model combined with reductive perturbation techniques to investigate the nonlinear electrostatic dynamics associated with phase-space electron holes observed near the upper mantle boundary of Venus. By imposing distinct boundary conditions, we derived two analytical nonlinear solutions describing both ion-acoustic solitary pulses and DL structures. The theoretical framework is consistent with *in situ* observations from VEX and PSP, which support the presence of compressive SWs and DL-type fluctuations in the Venusian magnetosheath.

Our analysis reveals six distinct phase-velocity modes arising from the compatibility condition, with ion-acoustic SWs propagating in the hydrogen frame and DL structures associated with the oxygen species. For solitary structures, the influence of plasma parameters on the electrostatic potential can be broadly categorised into stimulating parameters – namely ($\alpha, \sigma_{fe}, \sigma_{se}, \kappa$) – and inhibiting parameters – ($\psi, \sigma_H, u_{sp}^{(0)}$) – while a third group, including ($\delta, \omega, \sigma_{sp}, \sigma_O, \sigma_{te}, \sigma_{ke}, \beta$), exhibits negligible impact, as summarised in table 3. These solitary structures yield electric field amplitudes of $E \sim 20$ mV m^{-1}, pulse durations of $T \sim (2.5-4)$ ms and characteristic frequencies of $f \sim (0.4-5.6)$ kHz, in excellent agreement with PVO measurements (table 4).

In contrast, the DL structures display strong sensitivity to several plasma parameters, particularly α, ψ, δ, σ_{sp}, σ_{fe}, κ and $u_{sp}^{(0)}$, each of which reaches critical values beyond which the wave profile undergoes marked modification. Moreover, parameters such as σ_{fe}, σ_{se}, σ_{te} and α enhance the DL electrostatic potential amplitude, whereas others act to suppress it. The DL solutions predict electric fields of $E \sim 15$ mV m^{-1} and dominant frequency contributions near ∼1.5 kHz, consistent with PSP and PVO observations (table 4).

Our results further demonstrate, as illustrated in figure 1, that the linear phase velocity is independent of α, highlighting the insensitivity of small-amplitude waves to equilibrium parameters. However, nonlinear structures, including both SWs (figures 3 and 4) and DLs (figures 6–8), exhibit strong α dependence through modifications of the Sagdeev pseudopotential. This distinction demonstrates the fundamentally nonlinear nature of the structures studied here.

To conclude, the SWs and DL structures examined under different model configurations demonstrate notable agreement with PSP and PVO observations. Compared with the results of Morsi *et al*. (2024), reporting SWs with durations of ∼0.4 s and electric fields of 0.024–8 mV m^{-1}, our solitary structures are characterised by

https://doi.org/10.1017/S0022377826101846 Published online by Cambridge University Press

much shorter durations (∼3 ms), stronger amplitudes (∼20 mV m^{-1}) and higher frequencies (0.4–6 kHz). Similarly, our DLs exhibit durations of ∼4.5 ms and fields of ∼18 mV m^{-1}, compared with 0.16–0.35 mV m^{-1} and ∼1.6 ms reported in Morsi *et al*. (2024). These distinctions emphasise the strong sensitivity of nonlinear electrostatic structures to local plasma conditions and propagation geometry, and they reinforce the relevance of the present model in interpreting phase-space electron-hole phenomena in the Venusian magnetosheath.

Acknowledgements

S.M.S. acknowledges the support of the Alexander von Humboldt Foundation through a short research stay grant at Ruhr University Bochum, Germany. During the preparation of this work, the authors used Microsoft Copilot (https://copilot.microsoft.com/) for proofreading and language refinement.

Editor Antoine C. Bret thanks the referees for their advice in evaluating this article.

Funding

The publication of this article was funded by the Qatar National Library.

Declaration of interests

The authors report no conflict of interest.

REFERENCES

ABRAHAM, J.B. *et al.* 2022 Radial evolution of thermal and suprathermal electron populations in the slow solar wind from 0.13 to 0.5 au: Parker solar probe observations. *Astrophys. J.* **931**, 118.

AFIFY, M.S., ELKAMASH, I.S., SHIHAB, M. & MOSLEM, W.M. 2021 Evolution of ion-acoustic soliton waves in Venus's ionosphere permeated by the solar wind. *Adv. Space Res.* **67**, 4110–4120.

AKBARI, H. *et al.* 2022 Micro-scale plasma instabilities in the interaction region of the solar wind and the martian upper atmosphere. *J. Geophys. Res.: Space Phys.* **127**, e2022JA030591.

BARABASH, S. *et al.* 2007 The loss of ions from Venus through the plasma wake. *Nature* **450**, 650–653.

BLOCK, L.P. 1978 A double layer review. *Astrophys. Space Sci.* **55**, 59–83.

BOUGHER, S.W., HUNTEN, D.M. & PHILLIPS, R.J. 2022 *Venus II: Geology, Geophysics, Atmosphere, and Solar Wind Environment*. University of Arizona Press.

COLIN, L. 1980 The pioneer venus program. *J. Geophys. Res.: Space Phys.* **85**, 7575–7598.

DAS, G.C. 1979 Ion-acoustic solutions and shock waves in multicomponent plasmas. *Plasma Physics* **21**, 257.

DAS, G.C., PAUL, S.N. & KARMAKAR, B. 1986 Ion-acoustic solitary waves in two-temperature electron plasmas. *Phys. Fluids* **29**, 2192–2195.

DAS, G.C. & TAGARE, S.G. 1975 Propagation of ion-acoustic waves in a multi-component plasma. *Plasma Physics* **17**, 1025.

DÖNMEZ, O. & DAĞHAN, D. 2017 Analytic solutions of the Schamel-KdV equation by using different methods: application to a dusty space plasma. *Süleyman Demirel Üniversitesi Fen Bilimleri Enstitüsü Dergisi* **21**, 208–215.

EL-LABANY, S.K., EL-WARRAKI, S.A. & MOSLEM, W.M. 2000 Cylindrical ion-acoustic waves in a warm multicomponent plasma. *J. Plasma Phys.* **63**, 343–353.

FRANZ, J.R., KINTNER, P.M., PICKETT, J.S. & CHEN, L.-J. 2005 Properties of small-amplitude electron phase-space holes observed by polar. *J. Geophys. Res.: Space Phys.* **110**, A09212.

FUTAANA, Y., WIESER, S., GABRIELLA, B., Stas, & LUHMANN, J.G. 2017 Solar wind interaction and impact on the venus atmosphere. *Space Sci. Rev.* **212**, 1453–1509.

GAMAL, A., MOSLEM, W.M., YOUSEF, M.S. & ELLITHI, A.Y. 2025 Phase space electron hole in the Venusian upper mantle boundary. *Sci. Rep.* **15**, 17724.

https://doi.org/10.1017/S0022377826101846 Published online by Cambridge University Press

GOODRICH, K.A. *et al.* Laila 2018 MMS observations of electrostatic waves in an oblique shock crossing. *J. Geophys. Res. Space Phys.* **123**, 9430–9442.

GOŁKOWSKI, M., HARID, V. & HOSSEINI, P. 2019 Review of controlled excitation of non-linear wave-particle interactions in the magnetosphere. *Front. Astron. Space Sci.* **6**, 2.

HADID, L.Z. *et al.* 2021 Solar orbiter's first venus flyby: observations from the radio and plasma wave instrument. *Astron. Astrophys.* **656**, A18.

HOLMES, J.C., ERGUN, R.E., NEWMAN, D.L., AHMADI, N., ANDERSSON, L., LE CONTEL, O., TORBERT, R.B., GILES, B.L., STRANGEWAY, R.J. & BURCH, J.L. 2018 Electron phase-space holes in three dimensions: multispacecraft observations by magnetospheric multiscale. *J. Geophys. Res.: Space Phys.* **123**, 9963–9978.

HUBA, J.D. 1993 Generation of waves in the Venus mantle by the ion acoustic beam instability. *Geophys. Res. Lett.* **20**, 1751–1754.

HULTQVIST, B. 1971 On the production of a magnetic-field-aligned electric field by the interaction between the hot magnetospheric plasma and the cold ionosphere. *Planet. Space Sci.* **19**, 749–759.

HUTCHINSON, I.H. 2017 Electron holes in phase space: What they are and why they matter. *Phys. Plasmas* **24**, 055601.

KAKAD, B., KAKAD, A. & OMURA, Y. 2014 Nonlinear evolution of ion acoustic solitary waves in space plasmas: fluid and particle-in-cell simulations. *J. Geophys. Res.: Space Phys.* **119**, 5589–5599.

KAMALAM, T., SINGH, S.V., SREERAJ, T. & LAKHINA, G.S. 2023 Kinetic study of ion acoustic waves in Venusian ionosphere. *Phys. Plasmas* **30**, 072901.

KNORR, G. & GOERTZ, C.K. 1974 Existence and stability of strong potential double layers. *Astrophys. Space Sci.* **31**, 209–223.

KNUDSEN, W.C., JONES, D.E., PETERSON, B.G., KNADLER, J. & CHARLES, E. 2016 Measurement of solar wind electron density and temperature in the shocked region of Venus and the density and temperature of photoelectrons within the ionosphere of Venus. *J. Geophys. Res.: Space Phys.* **121**, 7753–7770.

KUZICHEV, V., IV, AGAPITOV, I.Y., MOZER, O.V., FS, & ARTEMYEV, A.V. 2017 Evolution of electron phase space holes in inhomogeneous magnetic fields. *Geophys. Res. Lett.* **44**, 2105–2112.

LAZAR, M. 2012 The electromagnetic ion-cyclotron instability in bi-Kappa distributed plasmas. *Astron. Astrophys.* **547**, A94.

LAZAR, M., PIERRARD, V., POEDTS, S. & FICHTNER, H. 2020 Characteristics of solar wind suprathermal halo electrons. *Astron. Astrophys.* **642**, A130.

LUHMANN, J.G. 1986 The solar wind interaction with Venus. *Space Sci. Rev.* **44**, 241–306.

LUHMANN, J.G., RUSSELL, C.T., SCHWINGENSCHUH, K. & YEROSHENKO, Y. 1991 A comparison of induced magnetotails of planetary bodies: Venus, Mars, and Titan. *J. Geophys. Res.: Space Phys.* **96**, 11199–11208.

LUNDIN, R., BARABASH, S., FUTAANA, Y., SAUVAUD, J.-A., FEDOROV, A. & PEREZ-DE TEJADA, H. 2011 Ion flow and momentum transfer in the Venus plasma environment. *Icarus* **215**, 751–758.

MAHAJAN, K.K. & DWIVEDI, A.K. 2004 Ionospheres of Venus and Mars: a comparative study. *Adv. Space Res.* **33**, 145–151.

MAKSIMOVIC, M. *et al.* 2005 Radial evolution of the electron distribution functions in the fast solar wind between 0.3 and 1.5 AU. *J. Geophys. Res.: Space Phys.* **110**, A09104.

MALASPINA, D.M. *et al.* 2020 Plasma double layers at the boundary between venus and the solar wind. *Geophys. Res. Lett.* **47**, e2020GL090115.

MALASPINA, D.M., ANDERSSON, L., ERGUN, R.E., WYGANT, J.R., BONNELL, J.W., KLETZING, C., REEVES, G.D., SKOUG, R.M. & LARSEN, B.A. 2014 Nonlinear electric field structures in the inner magnetosphere. *Geophys. Res. Lett.* **41**, 5693–5701.

MORSI, S.A., FAYAD, A.A., TOLBA, R.E., FICHTNER, H., LAZAR, M. & MOSLEM, W.M. 2024 Propagation of nonlinear ion-acoustic fluctuations in the mantle of Venus. *Astron. Astrophys.* **685**, A17.

PICKETT, J.S., MENIETTI, J.D., GURNETT, D.A., TSURUTANI, B., KINTNER, P.M., KLATT, E. & BALOGH, A. 2003 Solitary potential structures observed in the magnetosheath by the cluster spacecraft. *Nonlinear Proc. Geoph.* **10**, 3–11.

https://doi.org/10.1017/S0022377826101846 Published online by Cambridge University Press

ROSENAU, P. 1997 On nonanalytic solitary waves formed by a nonlinear dispersion. *Phys. Lett. A* **230**, 305–318.

RUBIA, R., SINGH, S.V., LAKHINA, G.S., DEVANANDHAN, S., DHANYA, M.B. & KAMALAM, T. 2023 Electrostatic solitary waves in the venusian ionosphere pervaded by the solar wind: a theoretical perspective. *Astrophys. J.* **950**, 111.

SALEM, S., FAYAD, A.A., EL-SHAFEAY, N.A., SAYED, F.S.H., SHIHAB, M., FICHTNER, H., LAZAR, M. & MOSLEM, W.M. 2022 Effect of the solar wind on the nature of arbitrary amplitude ion-acoustic solitary waves in Venus' upper ionosphere. *Mon. Not. R. Astron. Soc.* **517**, 2876–2893.

SAYED, F.S.H., TURKY, A.A., KORAMY, R.A. & MOSLEM, W.M. 2020 Nonlinear ion-acoustic waves at Venus ionosphere. *Adv. Space Res.* **66**, 1276–1285.

SCARF, F.L., TAYLOR, W.W.L. & GREEN, I.M. 1979 Plasma waves near venus: initial observations. *Science* **203**, 748–750.

SCARF, F.L., TAYLOR, W.W.L., RUSSELL, C.T. & BRACE, L.H. 1980*a* Lightning on Venus: orbiter detection of whistler signals. *J. Geophys. Res.: Space Phys.* **85**, 8158–8166.

SCARF, F.L., TAYLOR, W.W.L., RUSSELL, C.T. & ELPHIC, R.C. 1980*b* Pioneer venus plasma wave observations: the solar wind-venus interaction. *J. Geophys. Res.: Space Phys.* **85**, 7599–7612.

SCHAMEL, H. 1972 Stationary solitary, snoidal and sinusoidal ion acoustic waves. *Plasma Physics* **14**, 905.

SCHAMEL, H. 1973 A modified Korteweg-de Vries equation for ion acoustic wavess due to resonant electrons. *J. Plasma Phys.* **9**, 377–387.

SCHAMEL, H. 1986 Electron holes, ion holes and double layers: electrostatic phase space structures in theory and experiment. *Phys. Rep.* **140**, 161–191.

SHAABAN, S.M., KENNIS, S., LAZAR, M., PIERRARD, V. & POEDTS, S. 2025 Core-Halo correlations of solar wind electrons and temperature anisotropy instabilities. *J. Geophys. Res.: Space Phys.* **130**, e2025JA033838.

SHAABAN, S.M., LAZAR, M., LÓPEZ, R.A. & POEDTS, S. 2020 Electromagnetic ion–ion instabilities in space plasmas: effects of suprathermal populations. *Astrophys. J.* **899**, 20.

SOLIMAN, G.H., ZAHRAN, M.A. & ELKAMASH, I.S. 2023 Effect of trapping and reflection on dust acoustic solitary waves in nonthermal opposite polarity dust plasmas. *Phys. Scripta* **98**, 115617.

SPENNER, K., KNUDSEN, W.C., MILLER, K.L., NOVAK, V., RUSSELL, C.T. & ELPHIC, R.C. 1980 Observation of the Venus mantle, the boundary region between solar wind and ionosphere. *J. Geophys. Res.: Space Phys.* **85**, 7655–7662.

STRANGEWAY, R.J. 1991 Plasma waves at Venus. *Space Sci. Rev.* **55**, 275–316.

STRANGEWAY, R.J. & CRAWFORD, G.K. 1993 On the instability and energy flux of lower hybrid waves in the Venus plasma mantle. *Geophys. Res. Lett.* **20**, 1211–1214.

ŠTVERÁK, S., TRÁVNÍČEK, P., MAKSIMOVIC, M., MARSCH, E., FAZAKERLEY, A.N. & SCIME, E.E. 2008 Electron temperature anisotropy constraints in the solar wind. *J. Geophys. Res.: Space Phys.* **113**, A03103.

TAGARE, S.G. & CHAKRABARTI, A. 1974 Solution of a generalized Korteweg—de Vries equation. *Phys. Fluids* **17**, 1331–1332.

TAYLOR JR., H.A., BRINTON, H.C., BAUER, S.J., HARTLE, R.E., CLOUTIER, P.A. & DANIELL JR., R.E. 1980 Global observations of the composition and dynamics of the ionosphere of Venus: Implications for the solar wind interaction. *J. Geophys. Res.: Space Phys.* **85**, 7765–7777.

TITOV, D.V. *et al.* 2006 Venus express science planning. *Planet. Space Sci.* **54**, 1279–1297.

WASHIMI, H. & TANIUTI, T. 1966 Propagation of ion-acoustic solitary waves of small amplitude. *Phys. Rev. Lett.* **17**, 996.

YADAV, V.K. 2022 Viper: A plasma wave detection instrument onboard indian venus orbiter spacecraft. In *2022 URSI Regional Conference on Radio Science (USRI-RCRS)*, pp. 1–4. IEEE.

https://doi.org/10.1017/S0022377826101846 Published online by Cambridge University Press